Aalto University School of Science and Technology
CFD-group/ Department of Applied Mechanics

MEMO No   CFD/MECHA-6-2010   DATE: September 8, 2010

TITLE

Fluid–Structure Interaction with Low-Re Turbulence Model

AUTHOR(S)
Md Mizanur Rahman
Aalto University School of Science and Technology
Department of Applied Mechanics, CFD Group

ABSTRACT

This report presents a methodology to couple fluid and structure that gives rise to a variety of phenomena with applications in many areas, such as stability analysis of airplane wings, turbomachinery/bridge design and blood flow through arteries. An efficient interface for the fluid-structure coupling is developed that resolves complications associated with the interaction between two simulation modules. The computational framework consists of a multi-block moving grid technique, the low-Re k–ϵ turbulence model, and a structure/pressure-based flow solver. The moving grid approach which handles the geometric variations in time, combines master/slave strategy and transfinite interpolation techniques. A modified Newmark–β method is used for solving the non-linear structural equation.

MAIN RESULT

The turbulent flow characteristics subjected to a favorable pressure gradient inside a two/three–dimensional contraction have been carried out numerically. Attention is focused on the relaminarization in the boundary layer of a flat plate (i.e.,vane), positioned at the centerline of the contraction and the downstream development of the vortex induced vibration (VIV). FINFLO handles this complex case appreciably well.

PAGES
1–18

KEY WORDS
Finflo, $k - \epsilon$ model, vortex induced vibration, moving grid

APPROVED BY

Timo Siikonen   September 8, 2010

Introduction

Fluid and structure interaction (FSI) is important in many engineering disciplines, receiving growing interest as considerable progress has been made in computational fluid dynamics (CFD). For such problems, since the boundary shape is not known a priori, suitable computational strategies need to be developed to handle the issues involved. As the flow passes the vane (regarded as a flat plate or splitter plate with finite trailing edge thichness) trailing edge, fabricates three basic element: a wake, a shear layer separating from the body and a boundary layer developing on the body surface. The main challenge herein is that the flow typically experiences laminar–turbulent transition, causing lift–to–drag characteristics hard to predict and control [1]. The ideal two-dimensional vortex shedding is destroyed by increasing three–dimensionality due to streamwise vortices and to a larger extent by vortex dislocations [2]. The present study stems from an interest in understanding the fluid dynamics relevant to paper manufacturing.

A dynamically shaped rigid/flexible vane within a contracting channel is computationally studied. The channel is 700 mm long and 120 mm wide with a contraction ratio $9 : 1$. The vane is 600 mm long with Young modulus $E = 2200$ MPa, Poisson ratio $\nu = 0.375$ and density $\rho_p = 1200 \ kg/m^3$. The body of the vane is 540 mm long and the last 60 mm is tapered from the body thickness of 3 mm to the tip thichness $h = 1$ mm. A schematic view of the simplified computational model is given in Reference [2] with the vane hinged to the turbulence generator outlet, while the other end is free to move according to the flow conditions. The 2–D/3–D geometry is considered to assess the combined effects of inertial, elastic and aerodynamic forces on the movement of the fluid and solid boundaries. Several techniques are employed including multi-block grid, geometrical conservation laws and moving grid. Physical modeling issues involve turbulence modeling and turbulent–laminar transition.

In the current work, three cases of vortex induced vibration (VIV) are simulated: (a) 2–D simulation where the solid body movement is prescribed at the center of gravity, (b) 2–D simulation with the grid deformation and (c) 3–D simulation with the grid deformation. Herein, it is instructive to summarize alternative techniques dealing with coupled fluid/structure interactions. In handling fluid–structure interactions, three approaches have been proposed in the literature. The first one is the fully coupled method, which accounts for the fluid and structural dynamics via a single set of equations, and these governing equations are solved simultaneously [3]. The second approach and a widely used one, is to maintain the independence between the structure and fluid dynamics modules, and handle the passage of the force

loads and surface deformation information, between modules, after each time step [4]. The third approach employs a loosely coupled analysis, in which the structural model is updated infrequently, for example, the structure deflection is updated only after partial/full convergence of the CFD simulation, resulting in essentially a quasi-steady approach [5]. The present study follows the second approach.

The key development of the work presented in this paper is that a simplified fluid–structure model is incorporated. The turbulence–laminar flow field is predicted, while retaining the use of thin-plate mechanics to model flexible plate. The use of simulation permits arbitrary surface deformations of the vane to be accommodated and allows the development of VIV characteristics to be studied realistically. It is anticipated that no contribution from the shear stress is accounted for the aerodynamic forces on the flexible plate, because the plate motion is constrained to occur solely in the vertical direction. However, a full nonlinear flexible–plate model would, of course, permit motion in the horizontal direction due to both material extension/contraction in that direction and the geometric effects of large–amplitude deformations.

Fluid flow solver

The FINFLO employs cell centered finite-volume scheme combined with an artificial compressibility approach to solve the flow equations [6, 7]. A fully upwinded second-order spatial differencing is applied to approximate the convective terms. Roe's [8] damping term is used to calculate the flux on the cell face. A diagonally dominant alternating direction implicit (DDADI) time integration method [9] is applied for the iterative solution to the discretized equations. A multigrid method is utilized for the acceleration of convergence [10]. The basic implementation of the artificial compressibility method and associated features are described in [6, 7].

The code is extended to perform time-accurate calculations. Time-accuracy is achieved by using the dual-time method proposed by Jameson [11]. After being discretized in space by a finite-volume method, the time dependent Navier-Stokes equations can be written in the following semi-discrete form:

$$\frac{dw}{dt} + R(w) = 0 \tag{1}$$

where w is the vector of flow variables at each mesh point and R is the vector of the residuals, consisting of the spatially discretized flux balance of the Navier-Stokes equations. A second-order accurate fully implicit scheme

is then used to integrate the above equation in time [12]:

$$\frac{3w^{n+1} - 4w^n + u_i^{n-1}}{2\Delta t} + R\left(w^{n+1}\right) = 0 \tag{2}$$

Equation (2) can be reformulated as follows:

$$\frac{dw}{dt^*} + R^*(w) = 0, \qquad R^*(w) = \frac{3}{2\Delta t}w + R(w) - \frac{2}{\Delta t}w^n + \frac{1}{2\Delta t}w^{n-1} \tag{3}$$

where t^* is a pseudo–time. The solution of the implicit equation (2) is made equivalent to the steady state solution of Eq. (3) with the pseudo-time t^*. All acceleration techniques including the multigrid method can be applied that are already implemented in the steady FINFLO solver for solving Eq. (3). Once the solution to Eq. (3) converges in pseudo-time, the time accurate solution to Eq. (2) for one time step is achieved. In the calculations performed herein, 50 pseudo–time cycles are used for each real time step when coupled with the structural equation to ensure adequate convergence in pseudo–time.

Turbulence modeling

In collaboration with the Reynolds-averaged Navier-Stokes (RANS) equations, the proposed model determines the turbulence kinetic energy k and its dissipation rate ϵ by the following transport relations:

$$\frac{\partial \rho k}{\partial t} + \frac{\partial \rho u_j k}{\partial x_j} = \frac{\partial}{\partial x_j}\left[\left(\mu + \frac{\mu_T}{\sigma_k}\right)\frac{\partial k}{\partial x_j}\right] + \rho\, P - \rho\, \epsilon \tag{4}$$

$$\frac{\partial \rho \epsilon}{\partial t} + \frac{\partial \rho u_j \epsilon}{\partial x_j} = \frac{\partial}{\partial x_j}\left[\left(\mu + \frac{\mu_T}{\sigma_\epsilon}\right)\frac{\partial \epsilon}{\partial x_j}\right] + (C_{\epsilon 1}\, \rho\, P - C_{\epsilon 2}\, \rho\, \epsilon)/T_t \tag{5}$$

where μ implies the molecular viscosity, $\sigma_{(k,\epsilon)}$ are the appropriate turbulent Prandtl numbers and the production term $P = -\overline{u_i u_j}(\partial u_i/\partial x_j)$. The Reynolds stresses $\rho\overline{u_i u_j}$ are related to the mean strain–rate tensor S_{ij} through the Boussinesq approximation:

$$-\rho\overline{u_i u_j} = 2\,\mu_T\left(S_{ij} - \frac{1}{3}\,S_{kk}\,\delta_{ij}\right) - \frac{2}{3}\,\rho\, k\,\delta_{ij}, \qquad S_{ij} = \frac{1}{2}\left(\frac{\partial u_i}{\partial x_j} + \frac{\partial u_j}{\partial x_i}\right) \tag{6}$$

Since the viscous dissipation presumably dominates near the wall, the turbulent viscosity is evaluated from

$$\mu_T = \rho C_\mu\, f_\mu\, k\, T_t \tag{7}$$

4

where the model coefficient C_μ is in general a scalar function of the invariants formed on the strain rate S_{ij} and vorticity W_{ij} tensors in question:

$$S_{ij} = \frac{1}{2} \left(\frac{\partial u_i}{\partial x_j} + \frac{\partial u_j}{\partial x_i} \right), \quad W_{ij} = \frac{1}{2} \left(\frac{\partial u_i}{\partial x_j} - \frac{\partial u_j}{\partial x_i} \right) \tag{8}$$

The invariants of mean strain rate and vorticity tensors are defined by $S = \sqrt{2S_{ij}S_{ij}}$ and $W = \sqrt{2W_{ij}W_{ij}}$, respectively. The detailed functional form of C_μ is determined relying on the constraints such as realizability and appropriate experiments [13]:

$$C_\mu = \frac{3(1+\eta^2)\alpha_1}{3+\eta^2+6\eta^2\xi^2+6\xi^2}, \quad \eta = \alpha_2 T_t S, \quad \xi = \alpha_3 T_t W \tag{9}$$

The coefficients α_1–α_3 associated with Eq. (9) are given by

$$\begin{aligned}
\alpha_1 &= g\left(\frac{1}{4} + \frac{2}{3}\Pi_b^{1/2}\right), \quad \alpha_2 = \frac{3}{8\sqrt{2}}g \\
\alpha_3 &= \frac{3}{\sqrt{2}}\alpha_2, \quad g = \left(1 + 2\frac{P}{\epsilon}\right)^{-1}
\end{aligned} \tag{10}$$

where $\Pi_b = b_{ij}b_{ij}$ and the anisotropy of the Reynolds stress b_{ij} is defined as

$$b_{ij} = \frac{\overline{u_i u_j}}{2k} - \frac{1}{3}\delta_{ij} \tag{11}$$

Compatible relations for Π_b and P/ϵ are devised with the assistance of Reference [14] that depend nonlinearly on both the rotational and irrotational strains:

$$\Pi_b = C_\nu \frac{P}{\epsilon}, \quad \frac{P}{\epsilon} = C_\nu \psi^2 \tag{12}$$

with

$$C_\nu = \frac{1}{2\left(1 + T_t S\sqrt{1+R^2}\right)}, \quad \psi = T_t S \max(1, R) \tag{13}$$

where $R = |W/S|$ is a dimensionless parameter that is very useful to characterize the flow. For instance, for a pure shear flow $R = 1$, whereas for a plane strain flow $R = 0$.

The dynamic time scale k/ϵ is replaced by a realizable time scale T_t in Eq. (7) and can simply be defined as [15]

$$T_t = \sqrt{\frac{k^2}{\epsilon^2} + C_T^2 \frac{\nu}{\epsilon}} = \frac{k}{\epsilon}\sqrt{1 + \frac{C_T^2}{Re_T}}, \quad Re_T = \frac{k^2}{\nu\epsilon} \tag{14}$$
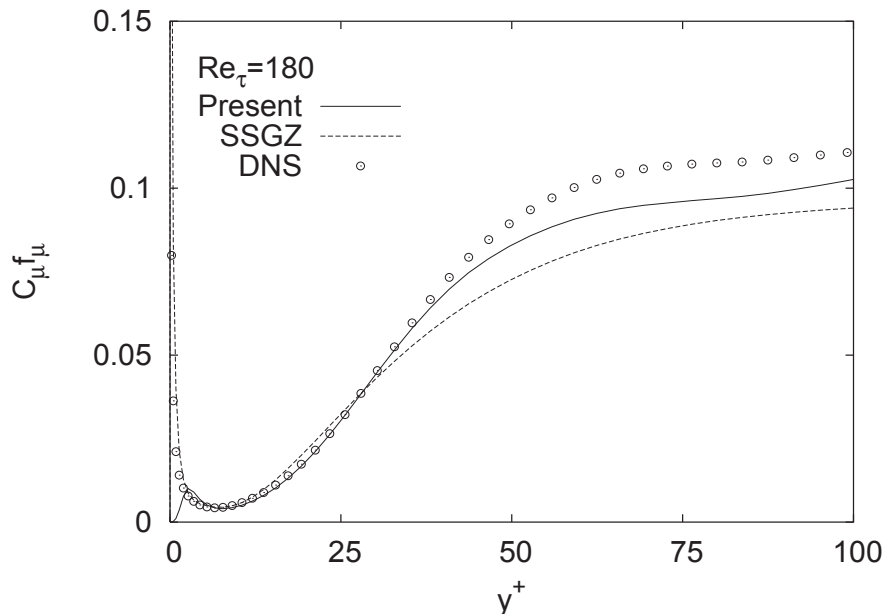
5

Figure 1: Variations of eddy viscosity coefficient with wall distance in channel flow.

where $\nu = \mu/\rho$ denotes the kinematic viscosity and Re_T is the turbulence Reynolds number. Equation (14) warrants that the eddy time scale never falls below the Kolmogorov time scale $C_T\sqrt{\nu/\epsilon}$, dominant in the immediate neighborhood of the solid wall. It prevents the singularity in the dissipation equation down to the wall. Alternatively, the turbulence time scale is k/ϵ at large Re_T but approaches the Kolmogorov limit $C_T\sqrt{\nu/\epsilon}$ for $Re_T \ll 1$. The empirical constant C_T associated with the Kolmogorov time scale is estimated as follows. In the viscous sublayer $k = y^2/(C_T^2\nu/\epsilon)$, where the basic scale is the Kolmogorov time scale. Besides, the k equation reduces to $\nu\partial^2 k/\partial y^2 = \epsilon$ as the wall is approached. Combining these relations provide $C_T = \sqrt{2}$. Obviously, the inclusion of T_t in the ϵ equation guarantees near-wall asymptotic consistency without resorting to *ad hoc* damping functions employed in many k–ϵ models [16].

The damping function included in Eq. (7) is chosen pragmatically as

$$f_\mu = 1 - \exp\left(-R_\lambda\right), \qquad R_\lambda = \frac{Re_y^{1.5}}{2\left(\psi + Re_T\right)} \tag{15}$$

where $Re_y = y\sqrt{k}/\nu$, another Reynolds number associated with the turbulence modeling. A plot of $C_\mu f_\mu$ against the DNS data [17] for a fully developed turbulent channel flow is shown in Fig. 1 and good correlation is

6

obtained. The result of the SSGZ model is also included in the figure for comparison. In this figure the abbreviation SSGZ stands for the model of So et al. [18]. The empirical function f_μ is valid in the whole flow field, including the viscous sublayer and the logarithmic layer. In the region close to the wall, the Reynolds stress $-\overline{uv} \sim y^3$ and $k \sim y^2$. To preserve the correct cubic power–law behavior of $-\overline{uv}$, the damping function (herein the product $C_\mu f_\mu$) needs to increase proportionally to y^{-1} in the near-wall region. Equation (15) confirms that as $Re_T > \psi$, $C_\mu f_\mu \sim y^{-1}$ in close proximity to the wall. As evinced by Fig. 1 in comparison with the DNS data, the adopted form of $C_\mu f_\mu$ reproduces the asymptotic limit involving the distinct effects of low–Reynolds number and wall proximity. The product $C_\mu f_\mu \approx 0.09$ (the standard choice for $C_\mu = 0.09$, pertaining to the linear k–ϵ model) remote from the wall to ensure that the model is compatible with the standard k–ϵ turbulence model. The use of $R_\lambda = R_\lambda(Re_y, Re_T)$ confronts the singularity at neither the separating nor the reattaching point in contrast to the adoption of $y^+ = u_\tau y / \nu$, where u_τ is the friction velocity. Consequently, the model is applicable to separated and reattaching flows.

Near–wall flows show a tendency to underestimate the dissipation rate ϵ due to the local anisotropy of turbulence, adhering to the non–dimensional parameter P/ϵ [19]. Researchers allow the coefficient $C_{\epsilon 1}$ to be a function of P/ϵ with a view to enhancing dissipation in such a situation [20, 21]. However, in some of the more complex flows that have been calculated, the dependence on P/ϵ prevents numerical convergence to a steady state [22]. One possible approach to counteracting this adverse situation is to explore alternative elements with relevance to P/ϵ:

$$f = 1 + \left(\frac{\Pi_b^2}{f_\mu}\right)^2, \quad C_{\epsilon 1} = \min(1.44\, f,\, C_{\epsilon 2}), \quad C_{\epsilon 2} = 1.9 - \left(\frac{\Pi_b}{C_T}\right)^2 \quad (16)$$

where $\Pi_b = \sqrt{b_{ij} b_{ij}} \approx C_\mu \psi$. As $f_\mu < 1$ in the near–wall region, the difference $(C_{\epsilon 2} - C_{\epsilon 1})$ becomes smaller that accounts for the additional production of dissipation by the anisotropy of turbulence. The parameter P/ϵ is supposed to serve the same purpose when included with $C_{\epsilon 1}$.

The budgets of k and ϵ from the DNS data suggest that the role of turbulent diffusion in the near–wall region is substantial. Accordingly, the coefficients $\sigma_{(k,\epsilon)}$ are modeled, rather than being assigned constant values (unlike the commonly adopted practice with $\sigma_k = 1.0$, and $\sigma_\epsilon = 1.3$):

$$\sigma_k = C_\mu + f_\mu, \qquad \sigma_\epsilon = C_T\, C_\mu + f_\mu \qquad (17)$$

The model coefficients $\sigma_{(k,\epsilon)}$ are developed such that sufficient diffusion is obtained in the vicinity of the wall. This contrivance tends to successfully predict the kinetic energy and dissipation rate profiles [23].

The transport equations for k and ϵ are subjected to the following boundary conditions at solid walls:

$$k_w = 0, \qquad \epsilon_w = 2\,\nu \left(\frac{\partial \sqrt{k}}{\partial y} \right)^2 \approx 2\,\nu \frac{k}{y^2} \tag{18}$$

To avoid numerical instability, the approximation for ϵ_w is applied at the first grid node neighboring the wall, rather than on the wall itself. This requires normal distance from a wall to the nearest grid point, which is unambiguous and readily available. The validity of Eq. (18) necessitates that the grid system is fine enough to produce the near–wall limiting behavior.

Structure solver

The fluid force obtained by solving the RANS equations is coupled with the motion of the vane. The structural motion subjected to VIV with one degree of freedom can be represented as

$$\ddot{u} + 2\zeta\omega\dot{u} + \omega^2 u = F \tag{19}$$

where u, $\dot{u}$ and $\ddot{u}$ are the displacement, velocity and acceleration of the vibrating plate, respectively. Other associated parameters are: the angular frequency ω, structural damping ζ and aerodynamic force F. The solution to the above equation can be obtained using the Newmark method [24]. Two major criteria are considered in choosing the appropriate scheme for time integration: stability and accuracy. It has been proved that Newmark method performs best fot $\Delta t/T < 0.01$, where T is the time period of vibrations [25] and hence time step size must be chosen appropriately to obtain best accuracy. A modified Newmark–β method is developed for solving Eq. (19). The formulae of Newmark–β method are given as follows:

$$\begin{pmatrix} u_{i+1} \\ \dot{u}_{i+1} \\ \ddot{u}_{i+1} \end{pmatrix} = H \begin{pmatrix} u_i \\ \dot{u}_i \\ \ddot{u}_i \end{pmatrix} + \frac{F_i}{mG} \begin{pmatrix} \beta\Delta t^2 \\ \gamma\Delta t \\ 1 \end{pmatrix} \tag{20}$$

where m is the mass of the body and G is given by

$$G = 1 + 2\zeta\omega\gamma\Delta t + \beta\omega^2\Delta t^2 \tag{21}$$

The matrix H is constructed as

$$H = \begin{pmatrix} 1 - \dfrac{\omega^2}{G}\beta\Delta t^2 & \Delta t\left(1 - \dfrac{2\zeta\omega + \omega^2\Delta t}{G}\beta\Delta t\right) & \dfrac{\Delta t^2}{2} - \dfrac{G+Q}{G}\beta\Delta t^2 \\[3mm] -\dfrac{\omega^2}{G}\gamma\Delta t & 1 - \dfrac{2\zeta\omega + \omega^2\Delta t}{G}\gamma\Delta t & \Delta t - \dfrac{G+Q}{G}\gamma\Delta t \\[3mm] -\dfrac{\omega^2}{G} & -\dfrac{2\zeta\omega + \omega^2\Delta t}{G} & -\dfrac{Q}{G} \end{pmatrix} \tag{22}$$

where Q is given by

$$Q = 2\zeta\omega(1-\gamma)\Delta t + \omega^2\left(\frac{1}{2}-\beta\right)\Delta t^2 \tag{23}$$

Note that γ and β are Newmark parameters that are chosen based on desired stability and accuracy. For the Newmark scheme to be unconditionally stable values of $\gamma = 0.5$ and $\beta = 0.25$ are chosen.

Deforming plate mechanics

The motion of the plate is modeled based on the classical thin–plate (length to thickness ratios of the order 20 or more) mechanics [26]:

$$\rho_p h\frac{\partial^2 u}{\partial t^2} + D\nabla^4 u = F, \qquad \nabla^4 = \frac{\partial^4}{\partial x^4} + 2\frac{\partial^4}{\partial x^2\,\partial z^2} + \frac{\partial^4}{\partial z^4} \tag{24}$$

where $\nabla^4 u$ is the fourth–order differential operator on the vertical plate displacement u. The parameters ρ_p, h and D are the density, thichness and flexible rigidity of the plate, respectively. The flexible rigidity is related to the elastic modulus E and the Poisson ratio ν through:

$$D = \frac{Eh^3}{12\left(1-\nu^2\right)} \tag{25}$$

The flexure term $\nabla^4 u$ of the vertical plate displacement can be written in central finite–difference form with a second–order approximation as

$$
\begin{aligned}
\nabla^4 u(x,z) \;=\; & \frac{1}{\lambda^4}\,[20u_{i,k} - 8\left(u_{i+1,k} + u_{i-1,k} + u_{i,k+1} + u_{i,k-1}\right) \\
& +2\left(u_{i+1,k+1} + u_{i+1,k-1} + u_{i-1,k+1} + u_{i-1,k-1}\right) \\
& +\left(u_{i+2,k} + u_{i-2,k} + u_{i,k+2} + u_{i,k-2}\right)]
\end{aligned}
\tag{26}
$$

where the algebraic length scale λ is evaluated as $\lambda = \sqrt{\Delta u^2 + \Delta x^2 + \Delta z^2}$ with $\Delta\phi(x,u,z)_n = \phi(x,u,z)_{n+1} - \phi(x,u,z)_{n-1}$ and $n=(i,j,k)$.

In this study, the built–in boundary conditions are enforced at the plate upstream edge while at the trailing edge the conditions of zero shear and bending moment are applied. Thus for a plate of streamwise length L yields:

$$u(0,t) = \nabla u(0,t) = 0, \qquad \nabla^2 u(0,L) = \nabla^3 u(0,L) = 0 \tag{27}$$

The free–end conditions are enforced by evaluating the flexure term $\nabla^4 u$ at u_n using two dummy nodes $n+1$ and $n+2$, beyond the end of the plate, whose displacements are found from the relations:

$$u_{n+1} = 2u_n - u_{n-1}, \qquad u_{n+2} = 3u_n - 2u_{n-1} \tag{28}$$

that are obtained from the discretized form of Equation (27) as described in Reference [26].

In principle, the damping effect is not included in Equation (24). Since the flexible plate may diverge due simply to the the magnitude of destabilizing aerodynamic forces, the damping is needed in order to stabilize the numerical scheme. Therefore, the discretized form of Equation (24) is converted to Equation (19) where the angular frequency ω at each nodal (computational) point can be evaluated from the linear differential equation [27]:

$$\frac{D}{\rho_p h}\nabla^4 u = \omega^2 u \tag{29}$$

with the above–mentioned boundary conditions. Note that Equation (24) is derived under the assumptions:

• the thickness of the plate is small compared with other dimensions
• no strain is suffered by the middle surface
• cross sections are plane before the strain and remain plane after the strain
• load is normal to the surface
• deflections are small in comparison with the thichness of the plate
• the influence of shear and rotating inertia is neglected
• the main fluid force that drives the plate motion remains the pressure difference between its upper and lower surfaces, $F = -\Delta p$, on the right-hand side of Equation (24).

Moving grid method

Since the structural movement needs to be accounted for in the fluid domain, one needs to ensure that the entire flow domain is remeshed appropriately. Therefore, an efficient moving mesh module is very important for performing unsteady flow calculations since the grid needs to be updated frequently. For multi–block grid movement, a method that combines master/slave strategy and transfinite interpolation techniques is suggested by Lian et al. [28]. The master/slave strategy is used to establish a relationship between the moving surface points (master points) and vertices located at the other blocks (slave points). The movement of the master points is based on the displacements obtained from the structure solver. The movement of the slave points depends on the movement of its surrounding master point. A slave point which has the coordinate of y^s, moves when its master point moves from y^m_{old} to y^m_{new}. A simple but effective formula suggested by Reference [29], based on spring analogy is given by

$$y^s_{new} = y^s_{old} + \alpha(y^m_{new} - y^m_{old}) \tag{30}$$

where the superscripts m and s represent master and slave, respectively, and α is the decay function:

$$
\begin{aligned}
\alpha &= \exp\{-\chi \min(500, ds/dm)\} \\
ds &= \sqrt{(x_{old}^s - x_{old}^m)^2 + (y_{old}^s - y_{old}^m)^2 + (z_{old}^s - z_{old}^m)^2} \\
dm &= \sqrt{(x_{new}^m - x_{old}^m)^2 + (y_{new}^m - y_{old}^m)^2 + (z_{new}^m - z_{old}^m)^2} \quad (31)
\end{aligned}
$$

The coefficient χ affects the stiffness. A larger χ causes the block to behave more like a rigid body and a smaller value makes the body behave like a softball. The value of $\chi = 1/64$ is normally used.

Solution algorithm

The solution procedure consists of the following steps:
• Solve the fluid flow equations.
• Evaluate the aerodynamic forces on the solid body.
• Solve the structural equation.
• Interpolate the solid body displacement to the fluid grid.
• Construct the new fluid grid.
• Repeat the above–mentioned steps.

Results for non–deforming plate

In this case, the plate is considered as a rigid body whose total mass is concentrated at the center of gravity (CG). It means that the CG (the whole body) moves in the vertical direction and the fluid grid is remeshed accordingly. The simulation input data are given below:
• $Re = 10700$, based on the free–stream velocity at the tip ($U_E = 10.7$ m/s) and tip thickness ($h = 1$ mm).
• $\rho = 0.432$ kg/m^3; $m_x = 0.2592$ kg; $E = 22 \times 10^8$ N/m^2.
• $\omega_x = \sqrt{k_x/m_x} = \sqrt{EA/(Lm_x)} \approx 2260$ Hz (Expt: 2180 Hz).
• Damping Ratio $\zeta = 1.0 \times 10^{-3}$; initial perturbation (displacement) $x = h/10.0 = 1.0 \times 10^{-4}$ m.
• Time step $\Delta t = 1.0/\omega_x \approx 4.6 \times 10^{-4}$ sec (used $\Delta t = 1.0 \times 10^{-4}$ sec).
• The lift force F_x acting in the vertical direction is evaluated as

$$
F_x(t) = C_x \sin(2\pi\omega_x t + \phi), \quad \phi = \tan^{-1}\left(\frac{2\zeta r}{1 - r^2}\right), \quad r = \frac{\omega_x}{\omega_n}
$$

• $C_x =$ amplitude of lift force.
• $\phi =$ phase angle between force and displacement.

- r = ratio of force frequency over undamped natural frequency.
- Dependence of force and displacement on $\sin(2\pi\omega_x t + \phi)$ and $x(t) = X\sin(2\pi\omega_x t)$ renders problem more manageable.
- Amplitude of vibration can be computed as

$$X = \frac{C_x}{k_x}\frac{1}{\sqrt{(1-r^2)^2 + (2\zeta r)^2}}$$

- Avoids the issue as far as the nature of randam fluctuations of lift, drag and amplitude are concerned.

Figures 2 and 3 exhibit the velocity and turbulence kinergy maps in the contracting channel. The contraction outlet velocity becomes approximately $2.7U_E$, U_E is the free stream velocity at the tip. Figure 3 shows a low turbulence intensity at the outlet. Computational results show (not shown here) that the acceleration through the contraction suppresses the relative turbulent intensities, which have almost no effect on the mean velocity distributions in the contraction. The streamwise component of the Reynolds stresses decays on passing through the contraction, whereas the transverse components grow equally. A reduction in the contraction angle brings about an increased decay rate of turbulence. Another phenomenon is the relaminarization of the turbulent boundary layer subjected to favorable pressure gradients due to acceleration in the contraction. Herein, the turbulent bursts near the wall disappear, the law of the wall breaks down and the turbulent intensity shows a tendency to decay. In principle, the shear stress distribution in the wall region rather than the Reynolds number is the most important factor for the occurrence of boundary layer relaminarization . The ultimate penalty due to the relaminarization is a significant reduction in the friction/heat transfer coefficients. Detailed presentations of the relaminarization phenomenon and associated features are provided with Reference [30].

The simulation of fluid-structure interaction as a function of time is shown in Figs. 4–6. Figure 4 shows the displacement and velocity of the vane body. Seemingly, the vibration dies out in time and the system is stable. Figures 5–6 exhibit the influence of vortices separating from the vane body.

Results for deforming plate

The simulation input data for two–dimensional deforming plate (vane) are given below:
- $Re = 10700$, based on the free-stream velocity at the tip ($U_E = 10.7$ m/s) and tip thickness ($h = 1$ mm).
- $\rho_p = 1200$ kg/m^3; $E = 22 \times 10^8$ N/m^2.

- ω is calculated at each nodal point using Eq. (29).
- Damping Ratio $\zeta = 0.01$; initial perturbation (displacement) $x = h/100.0 = 1.0 \times 10^{-5}$ m.
- Time step $\Delta t = 1.0 \times 10^{-4}$ sec.
- The lift force acting in the vertical direction is computed as $F = -\Delta p$.

Results that demonstrate the vortex induced vibration (VIV) as a function of time are shown in Figure 7. The deformation/movement of the vane body with time is obvious. A 224×1 non-uniform grid refinement is used around the solid body. It seems likely that more grid points are needed for smoothing the deformed surface of the vane. In addition, the use of boundary conditions, Eq. (28) damps out the vibration characteristics at the vane tip to a greater extent (i.e., the vane tip ceases to deform). However, it is clear that the numerical method permits arbitrary deformations of the flexible plate to be accommodated and allows the development of stable/unstable behavior to be studied as an initial–value problem.

The simulation input data for three–dimensional deforming plate are similar to the two–dimensional deformation case except the value of damping ratio ζ. In 3–D case $\zeta = 0.1$ is assigned that seemingly stabilize the numerical scheme. In principle, stability of aeroelastic interactions is of crucial importance. The attenuation of structural oscillations by both structural and aerodynamic damping characterizes stable flow–structure interactions. In an unstable situation, the motion–induced loading is further reinforced by the body motion, possibly leading to catastrophic failure. This unstable interaction involves extraction of energy from the fluid such that aerodynamic effects cancel structural damping. Flutter is the term applied to this unstable situation, which is a common design issue for long span structures. A nonuniform grid system having nearly 8.72 million cells with a large concentration of nodes in regions of steep gradients, such as those close to the walls is employed. Figure 8 shows the deformation/movement of the vane body as a function of time. To improve the accuracy of the interfacing the surface structural meshes are kept equal to fluids grids. However, similar impacts of the free–end boundary conditions as in 2–D case are observed that cause the vane tip to cease deformations. Investigation suggests that higher–order boundary conditions are needed to resolve this problem.

Conclusions

The computational methodology that couples a structure solver and a complex flow solver exhibits capabilities to predict flow and vibration characteristics in a convenient manner. The simulations have given insight into the flow

physics associated with performing a fluid–structure interaction computation over elastic bodies. Further challenge lies in developing the multi–block grid deforming method with the inclusion of separated flow effects and detailed structure modeling including nonlinear effects for other aeroelastic applications.

References

[1] Y Lian, J Steen, MT Wilander and W Shyy. Low Reynolds number turbulent flows around a dynamically shaped airfoil.*Computer & Fluid*, 32, 287-303, (2003).

[2] H Elornta. Fluid mechanics of the papermaking machine headbox – Instabilities and disturbances in the slice chamber. *Ph.D. Thesis*, Tampere University of Technology, Publication 572, (2005).

[3] GP Guruswamy and C Byum. Fluid-structure interactions using Navier-Stokes flow equations coupled with shell finite element structures. *AIAA Paper 93–3087*, July 1993.

[4] C Byum and GP Guruswamy. Comparative study of serial and parallel aeroelastic computations of wings. *NASA TM 108805*, January 1994.

[5] MJ Smith. Computational considerations of an Euler/Navier-Stokes aeroelastic method for a hovering rotor. *Journal of Aircraft*, 33, 429-434, (1996).

[6] Rahman MM, Rautaheimo P, Siikonen T. Numerical study of turbulent heat transfer from a confined impinging jet using a pseudo-compressibility method. *In Second International Symposium on Turbulence, Heat and Mass transfer*, Delft, The Netherlands, K. Hanjalic K, Peeters TWJ (eds). Delft University Press: Delft, 1997; 511-520.

[7] Rahman MM, Siikonen T. An artificial compressibility method for incompressible flows. *Numerical Heat Transfer, Part B* 2001; 40: 391-409.

[8] Roe PL. Approximate Riemann solvers, parameter vectors, and difference schemes. *Journal of Computational Physics* 1981; 43: 357-372.

[9] C. Lombard, J. Bardina, E. Venkatapathy and J. Oliger, Multi-dimensional formulation of CSCM - an upwind flux difference eigen-vector split method for the compressible Navier-Stokes equations. *In*

Sixth AIAA Computational Fluid Dynamics Conference , AIAA Paper 83-1895-CP, 1983; 649-664.

[10] Jameson A, Yoon S. Multigrid solution of the Euler equations using implicit schemes. *AIAA Journal* 1986; 24: 1737-1743.

[11] Jameson A. Time dependent calculations using multigrid with applications to unsteady flows past aerofoils and wings. *AIAA Paper 91-1596, 10th AIAA Computational Fluid Dynamics Conference*, June, 1991.

[12] J Hoffren, T Siikonen and S Laine. Conservative multiblock Navier-Stokes solver for arbitrarily deforming geometries. *Journal of Aircraft*, 32, 1342-1350, (1995).

[13] Rahman MM, Siikonen T. An eddy viscosity model with near-wall modifications. *International Journal for Numerical Methods in Fluids* 2005; 49: 975-997.

[14] Rahman MM, Siikonen T. Low-Reynolds number k–ϵ model for near-wall flow. *International Journal for Numerical Methods in Fluids* 2005; 47: 325-338.

[15] Rahman MM, Siikonen T. Near-wall turbulence modeling with enhanced dissipation. *International Journal for Numerical Methods in Fluids* 2003; 42: 979-997.

[16] Patel VC, Rodi W, Scheuerer G. Turbulence models for near-wall and low Reynolds number flow: A review. *AIAA Journal* 1985; 23:1308-1319.

[17] Mansour NN, Kim J, Moin P. Reynolds-stress and dissipation-rate budgets in a turbulent channel flow. *Journal of Fluid Mechanics* 1988; 194: 15-44.

[18] So RMC, Sarkar A, Gerodimos G, Zhang J. A dissipation date equation for low-Reynolds number and near-wall turbulence. *Theoretical and Computational Fluid Dynamics* 1997; 9: 47-63.

[19] Durbin PA, Speziale CG. Local anisotropy in strained at high Reynolds numbers. *Journal of Fluids Engineering* 1991; 113: 707-709.

[20] Ahn JW, Park TS, Sung HJ. Application of a near-wall turbulence model to the flows over a step with inclined wall. *International Journal of Heat and Fluid Flow* 1997; 18: 209-217.

[21] Durbin PA. A Reynolds-stress model for near-wall turbulence. *Journal of Fluid Mechanics* 1993; 249: 465-498.

[22] Durbin PA. Separated flow computations with k–ϵ–v^2 model. *AIAA Journal* 1995; 33: 659-664.

[23] Abe K, Kondoh T, Nagano Y. On Reynolds-stress expression and near-wall scaling parameters for predicting wall and homogeneous turbulent shear flows. *International Journal of Heat and Fluid Flow* 1997; 18: 266-282.

[24] Bahte KJ. Finite element procedures. *Englewood, cliffs NJ: Prentice-Hall*, 1996.

[25] Kamakoti R, Shyy W. Fluid-structure interaction for aeroelastic applications. *Progress in Aerospace Sciences* 2004; 40: 535-558.

[26] Balint TS, Lucey AD. Instability of a cantilevered flexible plate in viscous channel flow. *Journal of Fluids and Structures* 2005; 20: 893-912.

[27] Wu WX, Shu C, Wang CM. Mesh-free least-squares-based finite difference method for large amplitude vibration analysis of arbitrarily shaped thin plates. *Journal of Sound and Vibration* 2008; 317: 955-974.

[28] Lian Y, Shyy W, Viieru D, Zang B. Membrane wing aerodynamics for micro aerial vehicles. *Progress in Aerospace Sciences* 2003; 39: 425-465.

[29] Hartwich PM, Agrawal S. Method for perturbing multi-block patched grid in aeroelastic and design optimization applications. AIAA Paper 97-2038, 1983.

[30] Rahman MM, Siikonen T. Computation of turbulent flow characteristics in two-dimensional contraction with a new ASM. *Far East Journal of Applied Mathematics* 2004; 17: 243-276.